UNIVERSITÀ DEGLI STUDI DI PADOVA

DIPARTIMENTO DI BIOLOGIA

Corso di Laurea in Biotecnologie

ELABORATO DI LAUREA

COMPARATIVE ANALYSIS OF TWO-PHOTON ABSORPTION AND NORMAL ABSORPTION IMAGES OF DISPERSIONS OF β-$NaYF_4$:Yb^{3+},Er^{3+} NANOPARTICLES USING FLUORESCENCE AND TWO-PHOTON MICROSCOPES

Tutor: Prof. Antonio Barbon
Dipartimento di Scienze Chimiche

Laureando: Giovanni Vincenzo Cavallo

ANNO ACCADEMICO 2022/2023

Table of Contents

1 ABSTRACT

Up-conversion nanoparticles (UCNPs) have emerged as one of the most promising nanomaterials for bioanalytical and biomedical applications. β-$NaYF_4$:Yb^{3+},Er^{3+} nanoparticles, with a size less than 40 nm, are currently being studied for diagnostic applications, utilizing regular optical spectroscopies, exploiting their ability to absorb in the infrared (IR) and emit in the visible spectrum. In this study, we performed the first tests to explore the possibility of using them in emission microscopy. Fluorescence microscopy and imaging were employed as the first proof-of-concept to examine the detectability of these nanoparticles using different microscopes, using either normal absorption or two-photon absorption in the IR region, and to detect their emission in the visible spectrum.

2 INTRODUCTION

2.1 Lanthanoid-doped upconversion nanoparticles (UCNPs) - β-$NaYF_4$:Yb^{3+},Er^{3+} nanoparticles

Lanthanoid-doped up-conversion nanoparticles (UCNPs) represent a fascinating class of materials renowned for their ability to transform near-infrared excitation into visible emission, yielding background-free photoluminescence. Among these intriguing nanoparticles, the most commonly employed are UCNPs crafted from a $NaYF_4$ host matrix, and doped with Yb^{3+} ions as sensitizers, and Er^{3+} ions as activator. The sensitizers exhibit absorption characteristics around 980 nm into the near-infrared excitation range. The integration of Er^{3+} (or Tm^{3+}/ Ho^{3+}) ions as activators play an essential role in inducing up-conversion luminescence (UCL) within the ultraviolet−visible−near-infrared (UV−vis−NIR) spectral domains, the consecutive excitation of the lanthanoid Er^{3+} lead the system to a high energy state able to emit in the visible. [1]
Up-conversion nanoparticles (UCNPs) have emerged in the realm of bioimaging and diagnostics opening new pathway to explore. Particularly intriguing is their role as donors in Förster Resonance Energy Transfer (FRET) DNA hybridization assays. In combination with acceptor dyes such as Cy3.5, UCNPs offer a robust platform for probing molecular interactions and detecting DNA binding events. [2] Innovative analytical models have emerged to optimize UCNP-FRET DNA hybridization assays these models embrace diverse ion configurations within the nanoparticle core, introducing species like Nd^{3+} alongside the conventional Yb^{3+} as sensitizers. [3] (**Fig.1**.)

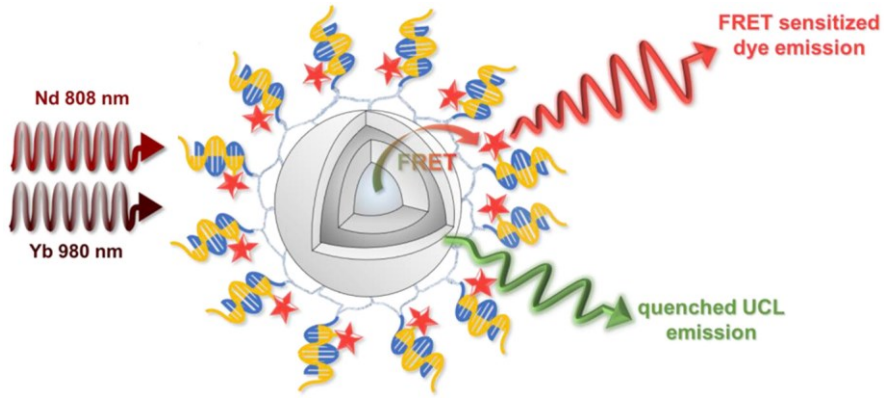

Fig.1. Exemplifying a prototypical UCNP-dye FRET DNA assay, this scenario involves DNA that bears a FRET acceptor dye (depicted as yellow DNA with a red star) and is hybridized with complementary DNA (illustrated in blue) located on the UCNP surface. Upon exciting the Nd^{3+} (808 nm) or Yb^{3+} (980 nm) sensitizers, energy transfer occurs from Er activators to dyes. Picture by the work of Pini et al. [3]

2.2 Multiphoton microscopy in biological imaging and diagnostic

Multiphoton microscopy (MPM) in the last thirty years has revolutionized the capabilities of biological imaging by the possibility of obtaining 3D-images, increased depth penetration and in-vivo imaging. Multiphoton microscopy principle is based on the phenomenon of multiphoton absorption. In the majority of the systems when two or more photons are absorbed simultaneously, their combined energy is sufficient to promote electrons to higher energy levels within a fluorophore. This principle enables the utilization of light with longer wavelengths compared to traditional fluorescence microscopy, such as near-infrared. Multiphoton processes such as two-photon excitation are referred to as “nonlinear” processes because the rate at which they occur depends non-linearly on the light intensity. For two-photon excitation there is an intensity -squared dependency: doubling the intensity produces four times the fluorescence. This process occurs within a tightly focused laser beam, where the photon density is significantly higher than in the surrounding regions (**Fig.2.**) To generate two-photon excitation a pulsed laser is used to increase the probability of two-photons absorption.[4] For the UCNPs, the upconversion occurs as due to successive (non-simultaneous) excitations. The correlation between excitation intensity and fluorescence is not simple to be determined as in two-photon absorption because the system undergoes to a set of processes (see further) some of which exhibit linear, other non-linear intensity dependance.

The in-vivo applicability, reduced phototoxicity compared to alternative fluorescence microscopy techniques, and enhanced tissue penetration capabilities of MPM make it a valuable tool for theranostic applications as image-guided drug delivery to tumor. [5].

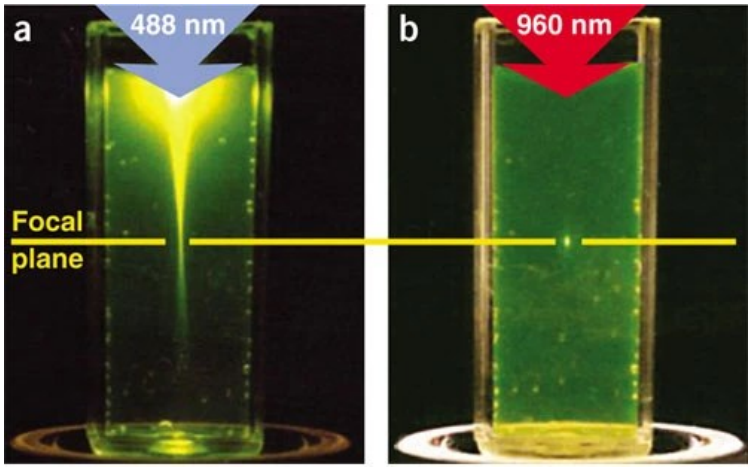

Fig.2. (a) Single-photon excitation of fluorescein by focused 488 nm light . **(b)** Two-photon excitation using focused femtosecond pulses of 960 nm light. Picture by the work of Zipfel et al. [4]

2.3 Up-conversion mechanism in Yb^{3+}-Er^{3+} system

In the UCNPs system the rare earth ion Yb^{3+} is used as a sensitizer since its special electronic structure consisting of only two energy levels within the 4f electrons, featuring a wide energy gap (as high as 10^4 cm^{-1}) and large absorption/emission cross sections. [6]

Er^{3+} ions are used as activators since they perform the up-conversion mechanism. The up-conversion mechanism upon excitation wavelength at 980 nm in the Yb^{3+}-Er^{3+} system results in green emission from Er^{3+} ions via a two-step process with sequential energy transfers from Yb^{3+} to Er^{3+}. Er^{3+} is excited first from $^4I_{15/2}$ to $^4I_{11/2}$ and then from $^4I_{11/2}$ to $^4F_{7/2}$ (requires two photons), the $^4F_{7/2}$ level relaxes non-radiatively to the thermalized emitting-states, $^2H_{11/2}$,$^4S_{3/2}$ (the green emitting states, $^2H_{11/2} \rightarrow {}^4I_{15/2}$ 520 nm, and $^4S_{3/2} \rightarrow {}^4I_{15/2}$ 540 nm). Red emission is a three-step process that requires three photons. The first two photon absorption are the same as for green emission, then a third photon excites Er^{3+} by energy transfer from $^4F_{7/2}$ to $^2G_{7/2}$, then it undergoes non-radiative relaxation to $^4G_{11/2}$. Finally, a backenergy transfer to Yb^{3+} occurs, leading to the transition down to $^4F_{9/2}$ (the red emitting state, $^4F_{9/2} \rightarrow {}^4I_{15/2}$ 660nm). A less significant blue emission also happens after relaxation from the $^2G_{7/2}$ state to the blue-emitting state $^2H_{9/2}$ ($^2H_{9/2} \rightarrow {}^4I_{13/2}$).(**Fig.3.**) [1]

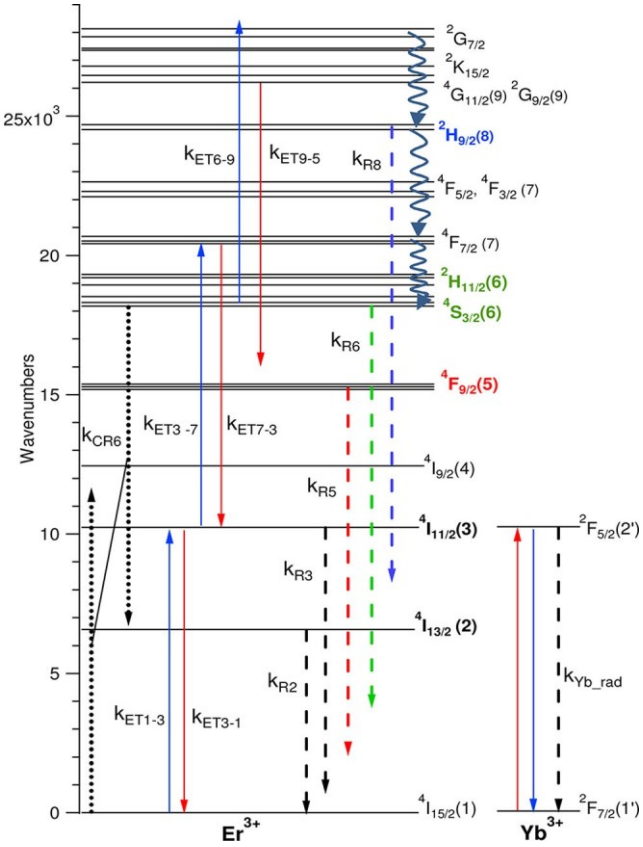

Fig.3.
Energy level diagram illustrating the essential steps in the (right panel) energy transfer up-conversion mechanisms. The $k_{ETx–y}$ represent rate constants for Yb–Er energy transfer, in both forward and back directions.
For further information and credit refer to the work of Anderson et al. [1]

2.4 Purpose of the thesis

UCNPs hold promise as versatile contrast agents and imaging probes due to their remarkable properties. These nanoparticles possess the capacity to absorb near-infrared (NIR) light and emit visible light, overcoming the limitations of tissue autofluorescence that can hinder imaging clarity. This property aligns perfectly with the capabilities of MPM, as the technique capitalizes on longer excitation wavelengths to achieve enhanced tissue penetration and resolution. It is intended to test the nanoparticles, if the visible emission can be observed by the fluorescence microscopes with excitation in the NIR.

The green-emitting state of Er^{3+} ions, $^2H_{11/2}$, has approximately a wavenumber of 19230,77 cm^{-1} which correspond to a wavelength approximately of 520 nm. [1] (**Fig.3**)
Half of this wavenumber correspond to 9615,39 cm^{-1} which correspond to a wavelength of 1040 nm. Conventional absorption bands of Yb^{3+} and Er^{3+} ions are not known within the 1020-1040 nm wavelength range. This range provides a pathway for a potential two-photon absorption process, wherein the simultaneous absorption of two low-energy photons induces an energy level transition in the Er^{3+} ions, after excitation with a pulsed laser within this wavelength range. The idea is that this two-photon absorption could lead to the direct population of the Er^{3+} energy level states $^2H_{11/2}$, (green emitting state), consequently, this process could trigger the emission of green light. This

hypothesis arises a potential for utilizing Er^{3+} two-photon absorption as a mechanism to achieve targeted controlled emissions in application involving UCNPs.

The one purpose of this thesis is to provide information about Er^{3+} two-photon absorption within the 1020-1040 nm range and targeted green emission, and to provide information about the detection of UCNPs at different concentrations for further theranostic applications.

3 MATERIALS AND METHODS

3.1 Preparation of nanoparticle dispersions

Six samples of Yb^{3+}:Er^{3+}-doped $NaYF_4$ nanoparticles were dispersed onto microscope slides at different concentrations (10 µg/mL x2; 50 µg/mL x1; 100 µg/mL x1; 250 µg/mL x1; 500 µg/mL x1).

The sample consists of colloidal core-shell upconverting nanoparticles (CS-UCNPs): the core, $NaYF_4$ doped with Yb^{3+} (20 mol%) and Er^{3+} (2 mol%) ions, is coated by a thin inert shell of $NaYF_4$. The nanoparticles were synthetized by a high-temperature colloidal procedure based on co-precipitation under controlled atmosphere. [3]

The different dispersions were prepared by dispersing the β-$NaYF_4$:Yb^{3+},Er^{3+} nanoparticles in toluene solvent. A drop of each prepared dispersion was then placed onto individual microscope slides and left to evaporate overnight. Following the preparation, because of lack of time only the higher concentration of 500 µg/mL and two lower concentrations of 10 µg/mL each were utilized for the objectives of this thesis.

3.2 Brightfield imaging

The imaging process was conducted using a Brightfield: ZEISS Axiophot brightfield microscope equipped with ZEISS EC Plan Neofluar 40x Ph2 Objective Lens (NA: 0,75), field of view (FOV): 256µm, resolution: 432 nm. Microscope slides with different nanoparticle dispersion (10 µg/mL; 500 µg/mL) were put under the 40x objective and images were acquired by the MikroCam II 20MP 1'' BRESSER camera.

3.3 Multiphoton imaging

For imaging, samples were mounted onto microscope slides and a drop of Type F Immersion liquid (RI: 1.52) was applied to each sample, then a cover slip was placed to cover the samples. The samples were visualized utilizing the Leica Stellaris 8 Dive multiphoton microscope (Leica Microsystems, Wetzlar, Germany), which was equipped with a HC IRAPO 25x, NA 1.00 water immersion Leica objective. Water was then added onto the cover slip to match the refraction indexes.

3.4 Image processing

FIJI [7] was employed for image processing and analysis purposes. It was used to take measurements of the area within brightfield images of nanoparticle

dispersions, and to evaluate the gray-value of the images acquired with the multiphoton microscope used as an indicator of the relative intensity of fluorescence emissions. The “mean pixel intensity” in this thesis is meant as the average grey-value of the pixel in the area measured. An application of the FIJI plugin “MorphoLibJ” [8] was used to identify clusters with larger areas in images acquired with the brightfield microscope.

4 Results

4.1 Brightfield images of nanoparticle clusters

Nanoparticles are too small (less than 40 nm [3]) to be seen directly under visible light (brightfield microscope employed resolution: 432 nm), but the images acquired using a brightfield microscope on the nanoparticle dispersions with concentrations of 500 µg/mL and 10 µg/mL revealed clusters that could be attributed to nanoparticle aggregation (**Fig. 4**).
Each image was captured using the same 40x objective, camera, and uniform criteria, resulting in an image size of 5440x3648 pixels and 256x171,5 µm.

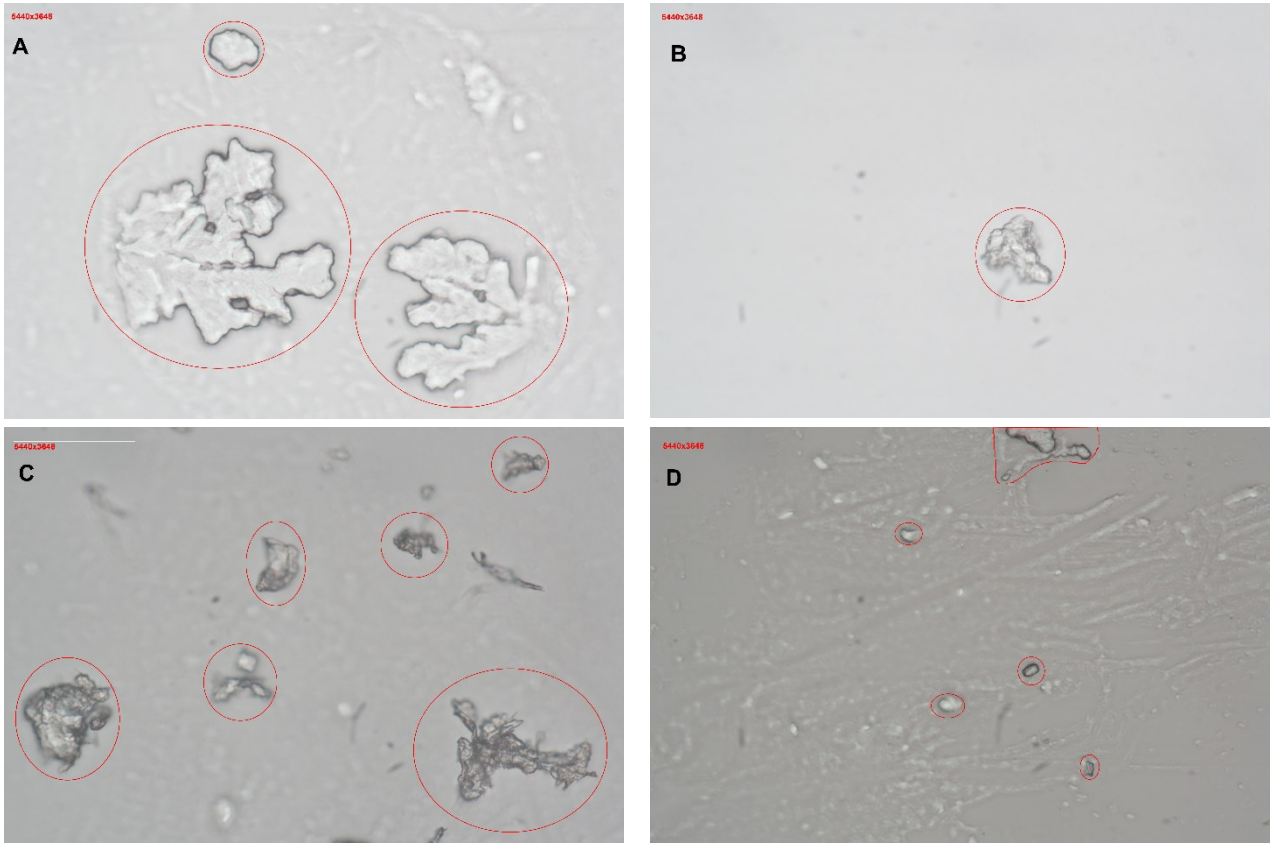

Fig. 4. Brightfield images of nanoparticles dispersions at different concentrations, the circles highlight clusters: **A)** image acquired of nanoparticle dispersion with concentration of 500µg/mL on microscope slide. **B)** image acquired in another region of the nanoparticle dispersion with concentration of 500µg/mL. **C)** image acquired of nanoparticle dispersion with concentration of 10µg/mL on microscope slide. **D)** image acquired in another region of the nanoparticle dispersion with concentration of 10µg/mL.

Employing the MorphoLibJ algorithm in FIJI to estimate the bigger cluster in each image and segment it, comparative pixel area measurements were conducted to quantify the dimensions of these clusters within each image (**Fig. 5**).
In dispersion with higher concentrations (500 µg/mL), bigger cluster areas were found to be 5231 μm^2 and 544,6 μm^2, in lower concentrations areas were 1200,5 μm^2 and 155,7 μm^2 (10 µg/mL).The results show that the cluster with the largest area formed at the highest concentration.

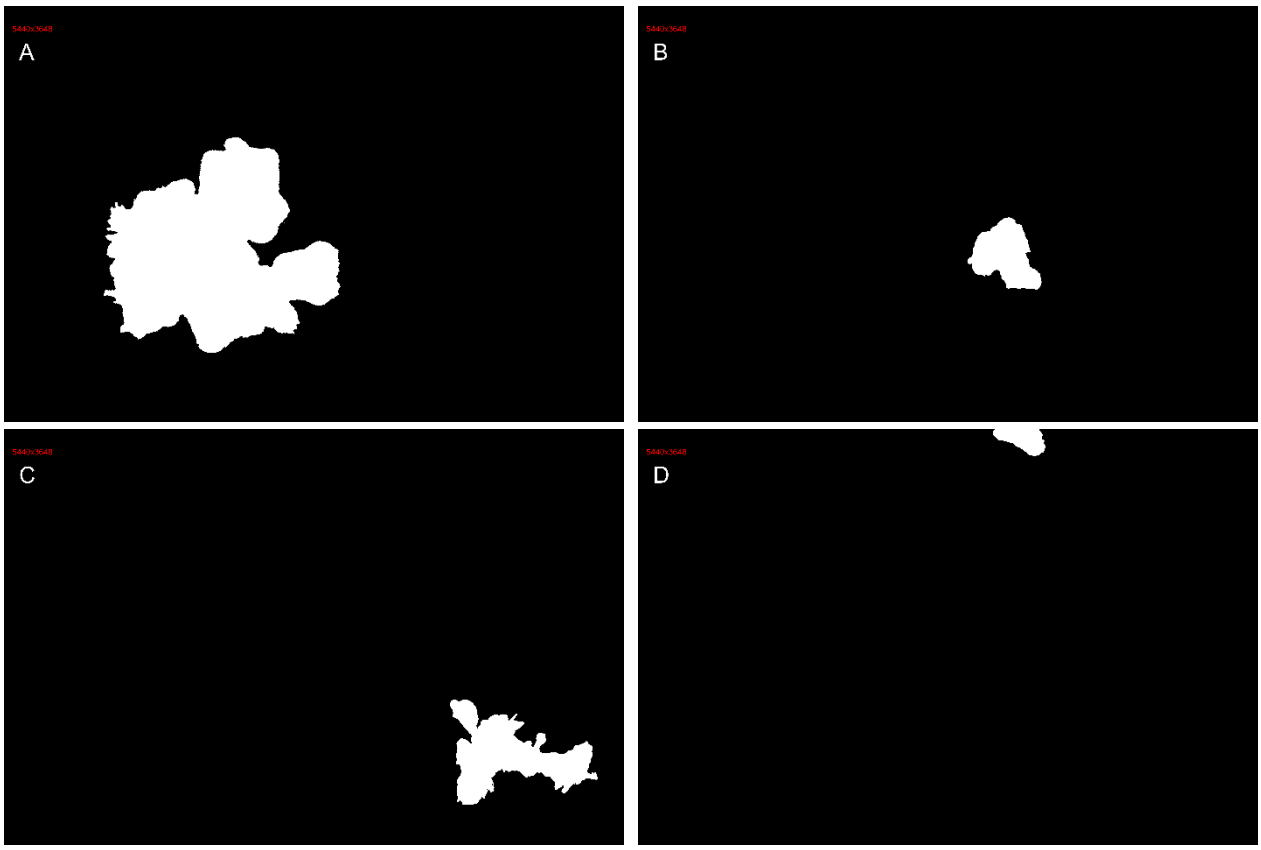

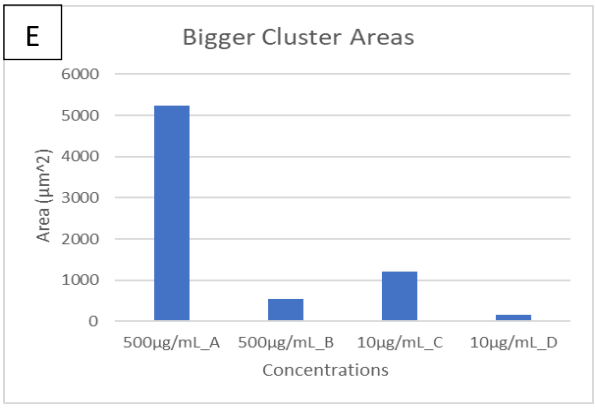

Fig. 5. Comparative measurements of the areas of the largest clusters at different concentrations, determined by the MorphoLibJ algorithm: **A)** Biggest cluster highlighted within nanoparticle dispersion with concentration of 500 µg/mL. **B)** Biggest cluster highlighted within another region of nanoparticle dispersion with concentration of 500 µg/mL. **C)** Biggest cluster highlighted within nanoparticle dispersion with concentration of 10 µg/mL. **D)** Biggest cluster highlighted within another region of nanoparticle dispersion with concentration of 10 µg/mL. **E)** The graph shows the areas.

Further analysis was conducted to investigate which concentrations had higher dispersion and lower cluster areas. Indicative clusters were selected as small clusters after excluding the biggest one revealed by the MorphoLibJ algorithm. The results revealed a trend of decreasing cluster areas with lower concentrations. (**Fig.6**) Further interpretations of the results follow in the discussion.

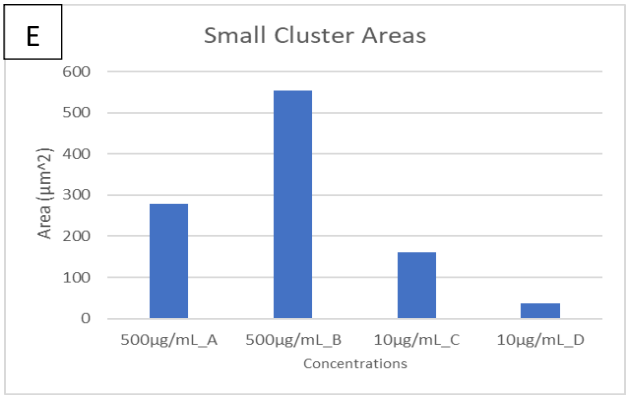

Fig.6. Areas of relatively smaller clusters at different concentrations selected after excluding the larger clusters identified by the MorphoLibGen plugin algorithm: **A)** Smallest cluster highlighted within nanoparticle dispersion with concentration of 500 µg/mL. **B)** Smallest cluster highlighted within nanoparticle dispersion with concentration of 500 µg/mL (it's also the biggest because there is only one cluster) **C)** Smallest cluster highlighted within nanoparticle dispersion with concentration of 10 µg/mL. **D)** Smallest cluster highlighted within nanoparticle dispersion with concentration of 10 µg/mL. **E)** The graph shows the areas.

4.2 Multiphoton microscope imaging and analysis

4.2.1 Excitation and Emission for 500 µg/mL Nanoparticle Dispersion

To explore the fluorescence characteristics of the nanoparticles, a series of three experiments were conducted on a nanoparticle dispersion with a concentration of 500 µg/mL. The purpose of these experiments was to elucidate the emissions of the nanoparticles under distinct excitation and detection conditions.
The first experiment aimed to capture a comprehensive view of the emission spectrum, providing insights into the nanoparticles' fluorescence behavior across a broad wavelength range.
In the second experiment, the purpose was to systematically explore the emission of nanoparticles with varying excitation wavelengths and to pinpoint specific emission peaks.
The third experiment purpose was to investigate the potential occurrence of two-photon absorption within the spectral range of 1020-1040 nm. (**Fig.8**)

Experiment #1: In the first experiment, the conventional and well-established excitation wavelength of 980 nm was employed, and emissions were detected within the range of 400-690 nm, with a step size of 10 nm. The results revealed distinct peaks of emission at 540 nm (green visible light spectrum) and 650nm (red visible light spectrum), indicating the presence of fluorescence in these regions upon excitation.

Experiment #2: The second experiment involved a wavelength scan across the wavelength range of 800-1000 nm, with a step size of 20 nm, and emissions detected at 548-564 nm. The aim was to ascertain the most efficient excitation wavelength within this range. The outcomes reaffirmed that the optimal excitation occurred at 980 nm, providing further support for the well-established excitation protocol.

Experiment #3: For the third experiment, a wavelength scan with an extended range of 900-1290nm using the multiphoton microscope, the detection was at 548-564 nm, utilizing a step size of 30nm. The primary objectives were to investigate the potential of two-photon absorption within the range of 1020-1050 nm and subsequent emission, and to explore any additional emissions following an excitation wavelength of 980 nm. The results indicated a slight fluorescence response at 1020 nm and no emissions beyond this wavelength.

The overall results demonstrated a generally higher intensity in emission following excitation at 980 nm, along with a slight emission at 1020 nm. However, this emission can be rationalized not as a result of double-photon absorption and subsequent excitation to the $^2H_{11/2}$ energy level, but rather as a regular absorption by the UCNPs. These nanoparticles exhibit a slight absorption even at that wavelength, as indicated by the absorption spectrum. (**Fig.7**)

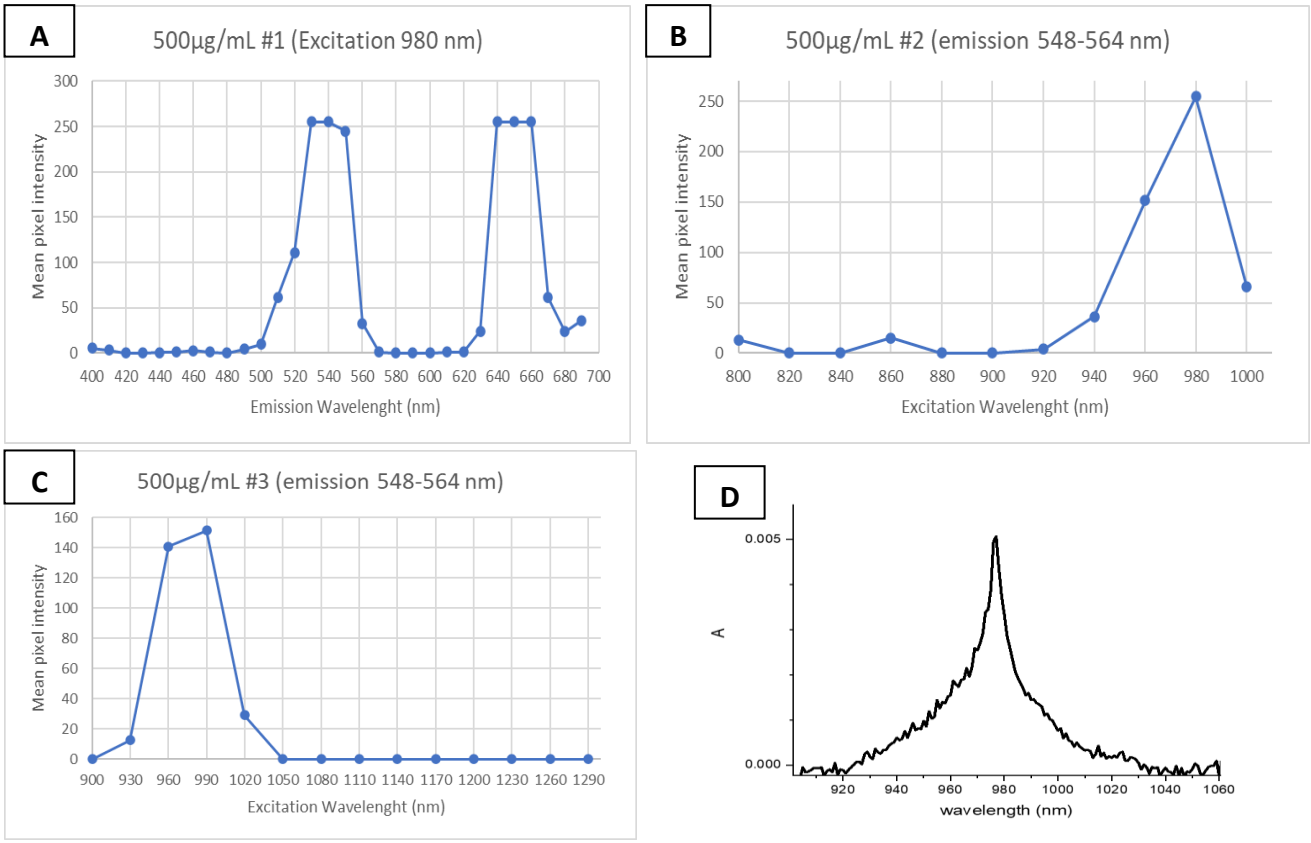

Fig.7. The graphs display the mean pixel intensity of the area highlighted, (in the 500µg/mL experiments) which is of 85,748 µm^2 (equivalent to 1050,997 pixels), using FIJI, along with the absorption spectrum of the nanoparticles . **A)** Emission detected at different wavelengths after excitation at 980 nm. **B)** Emission detected within the 548-564 nm wavelength range at different excitation wavelengths. **C)** Emission detected within the 548-564 nm wavelength range at different excitation wavelengths beyond the conventional 980 nm excitation wavelength. **D)** Absorption spectrum of a suspension of UCNP in toluene (1 mg/mL, 1 cm optical path).

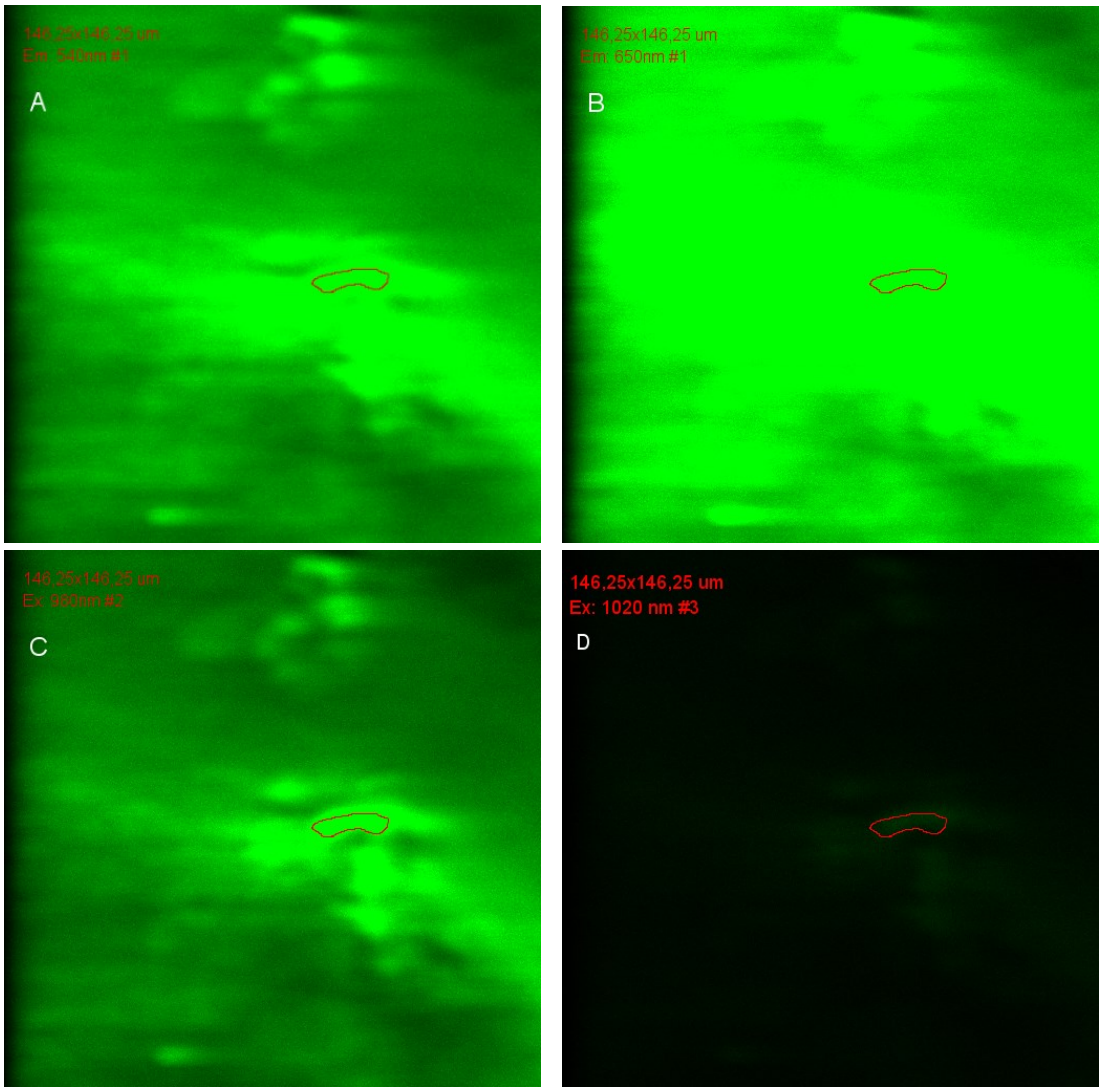

Fig.8. Emission images acquired by multiphoton microscope of nanoparticle dispersion with concentration of 500 µg/mL. Red closed lines highlight the same region at difference wavelengths and in different experiments and correspond to an area of 85,748 μm^2 and a pixel area of 1050,997: **A)** Wavelength emission at 540 nm with excitation at 980 nm. **B)** Wavelength emission at 650 nm (the image is green because the detection channel setup was on green) with excitation at 980 nm. **C)** Wavelength excitation at 980 nm and emission in the range of 548-564 nm during the wavelength scan experiment #2. **D)** Wavelength excitation at 1020 nm and emission in the range of 548-564 nm during the wavelength scan experiment

4.2.2 Excitation and Emission for 10 μg/mL Nanoparticle Dispersion

Three experiments were performed to investigate the emission characteristics of a 10 μg/mL nanoparticle dispersion under varying conditions utilizing a multiphoton microscope to acquire images. (**Fig.10**)

Experiment #1 In the first experiment, the conventional excitation wavelength of 980 nm was employed, and emissions were detected within the range of 400-690 nm, with a step size of 10 nm. The results indicated emissions at 540 nm (green visible light spectrum) and a higher intensity emission at 650 nm (red visible light spectrum). To enhance visibility, the relative laser intensity was increased, compared to the setup used for the experiments with the 500μg/mL concentration, from 2% to 14%. This experiment aimed to emphasize emission peaks and their visibility under the multiphoton microscope.

Experiment #2: The second experiment involved a wavelength scan within the range of 950-1060 nm, with a step size of 10 nm, and emission detection at 520-540 nm (green visible light spectrum). The objective was to investigate the possibility of two-photon absorption within the range of 1020-1050 nm and resulting emission. Additionally, the study examined emissions beyond an excitation wavelength of 980 nm. The results revealed a lower intensity emission, compared to the one with 980 nm, with excitation wavelength of 1020 nm, with no further emissions observed beyond this range.

Experiment #3: In the third experiment, a wavelength scan was conducted within the range of 950-1060 nm, employing a step size of 10 nm, and detecting emissions at 650-660nm (red visible light spectrum). Like the previous experiment, the focus was on investigating two-photon absorption within the 1020-1050 nm range and the corresponding emission. The outcomes shown a lower intensity emission, compared to the one with 980 nm, (though higher than the 520-540 nm emission under the same conditions) upon excitation at 1020 nm, with no emissions observed beyond this point.

A fourth experiment was conducted to investigate the absorption. at 1020 nm and its correlation with different laser intensity under the same setup as Experiment #2. In this case, a lower relative laser intensity (14% -> 8%) was used for another wavelength scan. The results revealed a linear correlation between intensity and emission (comparison with the results of Experiment #2), indicating that no two-photon absorption could be deduced. (**Fig.9**)
Mean pixel intensity (8% laser intensity): 4,700.
Mean pixel intensity (14% laser intensity): 9,451 (which is 2,011 times higher, showing an almost linear correlation with the laser intensity, which is 1,75 times higher, it was expected to be four times higher in the case of two-photon absorption).

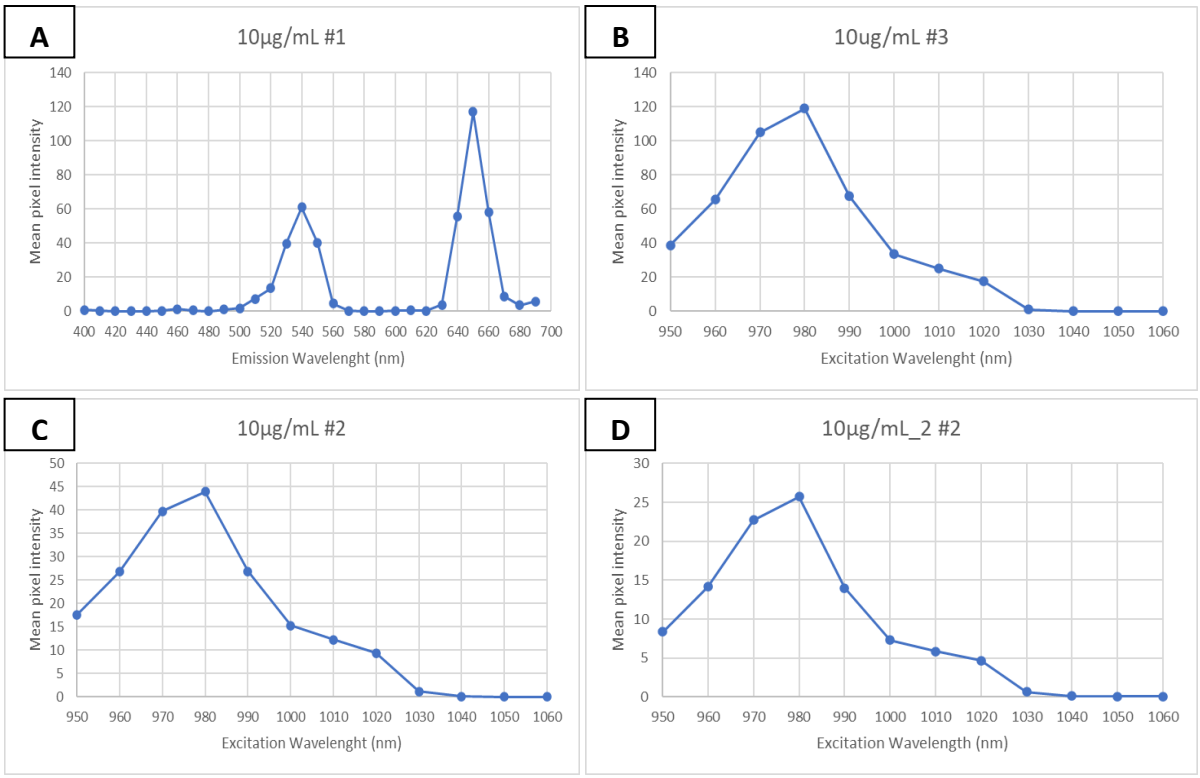

Fig.9. The graphs display the mean pixel intensity of the area highlighted (in the 10µg/mL experiments), which is of 253,387µm^2 (equivalent to 3105,715 pixel), using FIJI. **A)** Emission detected at different wavelengths after excitation at 980 nm. **B)** Emission detected within the 650-660 nm wavelength range at different excitation wavelengths. **C)** Emission detected within the 520-540 nm wavelength range at different excitation wavelengths with relative laser intensity at 14%. **D)** Emission detected within the 520-540 nm wavelength range at different excitation wavelengths with relative laser intensity at 8%.

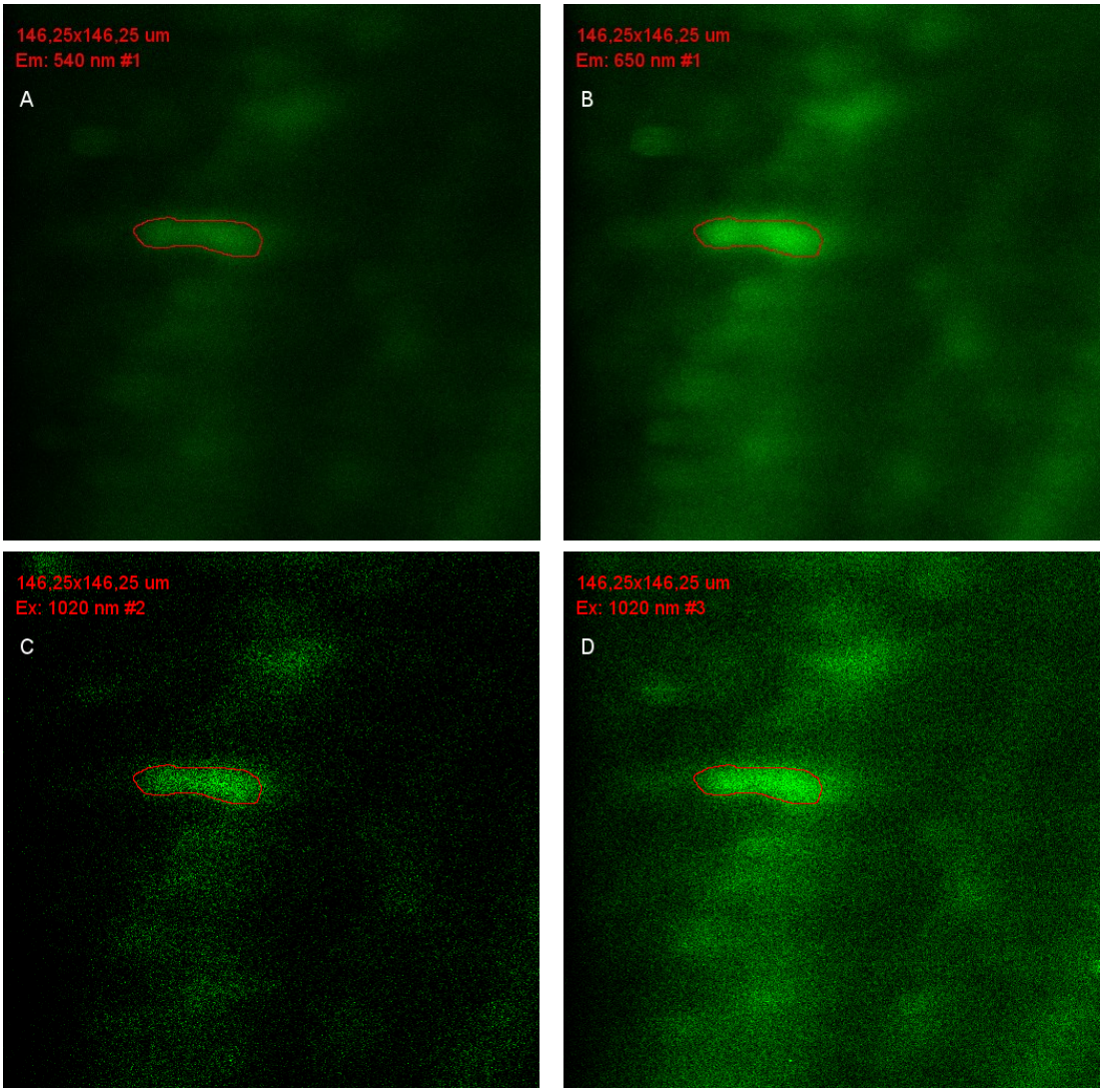

Fig.10. Emission images acquired by multiphoton microscope of nanoparticle dispersion with concentration of 10 µg/mL. Red closed lines highlight the same region at difference wavelengths and in different experiments and they correspond to an area of 253,387 μm^2 and a pixel area of 3105,715: **A)** Wavelength emission at 540 nm with excitation at 980nm. **B)** Wavelength emission at 650 nm (the image is green and not red because the detection channel setup was on green) with excitation at 980 nm. **C)** Wavelength excitation at 1020 nm and emission within the range of 520-540 nm during the wavelength scan experiment #2; to enhance visibility of the highlighted region, adjustments were made to the brightness and contrast settings, this operation resulted in an increase in noise. **D)** Wavelength excitation at 1020 nm and emission within the range of 650-660 nm during the wavelength scan experiment #3 (the image is green and not red because the detection channel setup was on green); to enhance visibility of the highlighted region, adjustments were made to the brightness and contrast settings, this operation resulted in an increase in noise.

5 Discussion

The brightfield observation of the nanoparticle dispersions revealed a larger cluster for the highest concentration and overall smaller clusters in the lower concentrations, indicating the potential influence of concentration on cluster formation. Smaller clusters imply a higher dispersion, which could prove valuable for potential future applications in cellular environments. The multiphoton results also demonstrated the detectability of these nanoparticle clusters at 10µg/mL, which due to their higher dispersion characteristics, are particularly suggested for further diagnostic developments.

Due to the limited analysis, further research is needed to explore the correlation between these nanoparticles and cluster formation; investigations are necessary also to study the emission and the cluster formation in a cellular environment.

Higher concentrations of β-$NaYF_4$:Yb^{3+},Er^{3+} nanoparticle dispersions required lower relative laser excitation intensity to have higher emission intensity and consequently better contrast than lower concentrations.

Experiments underlined the success of employing the well-established 980 nm excitation wavelength leading to better emissions at 540 nm and 650 nm than other excitation wavelengths in the NIR.

No blue emissions were detected, a possible cause could be the low emission intensity in the blue region of these nanoparticles.

Red emission (650 nm) intensity was higher than green emission (540 nm) intensity.

Experiments with focus turned to wavelength scanning within the 950-1060 nm range, aiming to understand two-photon absorption within the 1020-1050 nm interval and emission demonstrated a reduced, yet distinguishable emission upon excitation at 1020 nm, compared to 980 nm excitation, highlighting a possible two-photon absorption and excitation of the energy level state $^2H_{11/2}$ of Er^{3+} ions and consequently emission.

With this excitation we should expect a higher green emission [1] than red emission, but the results showed a higher red emission. Furthermore, the emission intensity appears to exhibit a linear correlation with the laser intensity, as demonstrated by the experiments. Due to these results, it cannot be concluded that two-photon absorption occurred. The absorption at 1020 nm could be attributed to the Yb^{3+} absorption spectrum, maybe broadened slightly by the electric field of the host matrix and environmental interactions. [6]

The results elucidate the detectable emissions at specific wavelengths, the impact of laser intensity on visibility, and the behavior of emissions under varying excitation conditions. Future research will be necessary to study the relationship between the different fluorescence intensities identified under the most sensitive conditions (excitation at 980 nm, emission at 650 nm) throughout the investigated area, and the various nanoparticle concentrations or clusters below the resolution limit of the microscope. This encourages the utilization of these nanoparticles in microscopy.

Bibliography

1. Robert B. Anderson, Steve J. Smith, P. Stanley May, and Mary T. Berry. The Journal of Physical Chemistry. Letters 2014 5 (1), 36-42. DOI: https://doi.org/10.1021/jz402366r

2. Francés-Soriano, L., Estebanez, N., Pérez-Prieto, J., & Hildebrandt, N. (2022). DNA-Coated Upconversion Nanoparticles for Sensitive Nucleic Acid FRET Biosensing. *Advanced Functional Materials*, *32*(37), 2201541. https://doi.org/10.1002/adfm.202201541

3. Pini, F.; Francés-Soriano, L.; Andrigo, V.; Natile, M. M.; Hildebrandt, N. Optimizing Upconversion Nanoparticles for FRET Biosensing. *ACS Nano* 2023, 17 (5), 4971– 4984, DOI: 10.1021/acsnano.2c12523

4. Zipfel, W., Williams, R. & Webb, W. Nonlinear magic: multiphoton microscopy in the biosciences. Nat Biotechnol 21, 1369–1377 (2003). https://doi.org/10.1038/nbt899

5. Fokong, S., Theek, B., Wu, Z., Koczera, P., Appold, L., Jorge, S., Resch-Genger, U., van Zandvoort, M., Storm, G., Kiessling, F., & Lammers, T. (2012). Image-guided, targeted and triggered drug delivery to tumors using polymer-based microbubbles. *Journal of Controlled Release*, *163*(1), 75-81. https://doi.org/10.1016/j.jconrel.2012.05.007

6. L. Xu , Y. Liu , Z. Zhou , X. Sun , I. Din , F. Khan , Y. Li , H. Li , J. Ren , J. Carvajal , J. Zhang and L. Liu , A new role of Yb^{3+}-an energy reservoir for lanthanide upconversion luminescence, *Nanoscale*, 2021, **13** , 9978 —9988. https://doi.org/10.1039/D0NR08205H

7. Schindelin, J., Arganda-Carreras, I., Frise, E., Kaynig, V., Longair, M., Pietzsch, T., … Cardona, A. (2012). Fiji: an open-source platform for biological-image analysis. *Nature Methods*, *9*(7), 676–682. doi:10.1038/nmeth.2019

8. Legland, D., Arganda-Carreras, I., & Andrey, P. (2016). MorphoLibJ: integrated library and plugins for mathematical morphology with ImageJ. *Bioinformatics*, *32*(22), 3532–3534. doi:10.1093/bioinformatics/btw413